

Energy & Environmental Science

Accepted Manuscript



This is an *Accepted Manuscript*, which has been through the Royal Society of Chemistry peer review process and has been accepted for publication.

Accepted Manuscripts are published online shortly after acceptance, before technical editing, formatting and proof reading. Using this free service, authors can make their results available to the community, in citable form, before we publish the edited article. We will replace this *Accepted Manuscript* with the edited and formatted *Advance Article* as soon as it is available.

You can find more information about *Accepted Manuscripts* in the [Information for Authors](#).

Please note that technical editing may introduce minor changes to the text and/or graphics, which may alter content. The journal's standard [Terms & Conditions](#) and the [Ethical guidelines](#) still apply. In no event shall the Royal Society of Chemistry be held responsible for any errors or omissions in this *Accepted Manuscript* or any consequences arising from the use of any information it contains.

1 **Multijunction Si photocathodes with tunable photovoltages from 2.0 V to 2.8 V for light**
2 **induced water splitting**

3 F. Urbain¹, V. Smirnov¹, J.-P. Becker¹, A. Lambertz¹, F. Yang², J. Ziegler², B. Kaiser², W.
4 Jaegermann², U. Rau¹, and F. Finger¹

5 ¹IEK-5 Photovoltaik, Forschungszentrum Jülich, D-52425, Jülich, Germany

6 ²Institute of Materials Science, TU Darmstadt, D-64287, Darmstadt, Germany

7

8

9 **Abstract**

10 We report on the development of high performance triple and quadruple junction solar cells
11 made of amorphous (a-Si:H) and microcrystalline silicon ($\mu\text{c-Si:H}$) for the application as
12 photocathodes in integrated photovoltaic-electrosynthetic devices for solar water splitting. We
13 show that the electronic properties of the individual sub cells can be adjusted such that the
14 photovoltages of multijunction devices cover a wide range of photovoltages from 2.0 V up to
15 2.8 V with photovoltaic efficiencies of 13.6 % for triple and 13.2 % for quadruple cells. The
16 ability to provide self-contained solar water splitting is demonstrated in a PV-biased
17 electrosynthetic (PV-EC) cell. With the developed triple junction photocathode in the a-
18 Si:H/a-Si:H/ $\mu\text{c-Si:H}$ configuration we achieved an operation photocurrent density of 7.7
19 mA/cm^2 at 0 V applied bias using a Ag/Pt layer stack as photocathode/electrolyte contact and
20 ruthenium oxide as counter electrode. Assuming a faradic efficiency of 100 %, this
21 corresponds to a solar-to-hydrogen efficiency of 9.5 %. The quadruple junction device
22 provides enough excess voltage to substitute precious metal catalyst, such as Pt by more
23 earth-abundant materials, such as Ni without impairing the solar-to-hydrogen efficiency.

24

25

26

27

28

29

30

31

32

33

34

35

36

37

38

39

40

41

42

43

I. Introduction

44 Efficient production of clean and storable chemical fuels, such as hydrogen, from solar energy
45 is of utmost importance for future sustainable post-carbon energy systems.^{1,2} It is therefore
46 vital to develop and improve efficient artificial processes to convert the energy of light into
47 chemical energy. For this purpose, photoelectrolysis of water by semiconductor based devices
48 represents a prominent route which recently raised increasing interest among research groups
49 worldwide.³⁻⁵ Photoelectrolysis of water is a chemical process that produces hydrogen (and
50 oxygen) and requires light induced potential differences, i.e. photovoltages over 1.6 V to run
51 autonomously, taking into account the overpotential losses in such systems.⁶ Among state-of-
52 the-art solar fuel generators, photovoltaic (PV)-biased electrochemical cells (denoted as PV-
53 EC devices hereafter), which consist of a solar cell, submerged in an electrolyte and
54 electrically arranged in series with electrocatalysts for the hydrogen (HER) and oxygen
55 evolution reaction (OER), respectively, offer several advantages compared to other
56 photoelectrochemical device configurations:⁷

- 57 • In a PV-EC device the photovoltage and the photocurrent generated by the underlying
58 solar cell are entirely available for the photoelectrolysis, i.e. the solar cell can be
59 adjusted independent from any electrochemical reaction at the solar cell/electrolyte
60 interface^{8,9} or any second photoactive electrode material.¹⁰
- 61 • Such flexibility, so far, allowed for higher achievable efficiencies compared to other
62 solar fuel generator configurations.¹¹
- 63 • The current-voltage characteristics of the electrocatalysts can be merged with the PV
64 characteristics of the solar cell, in terms of a simple series connection, to accurately
65 predict the PV-EC device performance.¹²⁻¹⁴

66 Among the semiconductor technologies used for solar water splitting, multijunction thin film
67 silicon solar cell structures have been explored for over 20 years now and have acquired a
68 leading position,^{10,15-19} thanks to their ability to provide high photovoltages in multijunction
69 structures above the required potential for photoelectrolysis.⁹ The highest reported solar-to-
70 hydrogen (STH) efficiencies for monolithic thin film silicon based solar fuel generators are
71 6.8 % for tandem¹² and 7.5 % and 7.8 %, respectively, for triple junction based
72 photoelectrodes made of hydrogenated amorphous silicon (a-Si:H).^{19,20} The thin film silicon
73 device concept allows to fabricate monolithic cells, which can be integrated in a compact
74 water splitting device. Other studies, in contrast, use module connections of several solar
75 cells, e.g. III-V based, CIGS, crystalline silicon, or perovskite solar cells,^{21,22,23,24} to provide
76 the sufficient voltage to run the HER and OER, respectively, without an external bias.
77 Although, the achieved STH efficiencies in module based water splitting devices are
78 remarkable,¹¹ the multijunction thin film silicon concept offers several advantages compared
79 to series connected solar cells: in general the series connection requires an additional
80 processing step (laser scribing or solar tabbing wire connection) compared to the monolithic
81 multijunction solar cell fabrication process, which becomes particularly relevant in industrial
82 applications. Additionally, series connected cells cannot be adjusted precisely with respect to
83 the specifically needed photovoltage of the complete system, which varies with the
84 overpotentials of the used catalysts for the HER and OER, respectively. Considering that the
85 photocurrent at the respective required voltage determines the STH efficiency,⁶ the

86 photovoltage/photocurrent tradeoff, prevented higher STH efficiencies so far. In crystalline
87 silicon solar cells, for instance, the photovoltage can be adjusted only in large steps of approx.
88 600 mV by connecting several cells in series. However, in such case the increase in voltage is
89 accompanied by a significant decrease in photocurrent and device efficiency (if the active
90 solar cell area remains unchanged). The same however also applies to multijunction solar
91 cells made merely of amorphous silicon alloys (a-Si:H and a-Si:Ge:H), which have been
92 applied for unbiased solar water splitting by Delahoy et al. and Khaselev et al. for
93 instance^{15,20}. Therefore, it is crucial to develop solar cells with the ability to tune the
94 photovoltage not only in large but also in small steps in order to fulfill the particular
95 requirements of various PV-EC systems. At the same time a change in the photovoltage
96 should ideally not impair the device efficiency.

97
98 This task can be performed by monolithic multijunction solar cells made of thin films of
99 amorphous (a-Si:H) and microcrystalline ($\mu\text{c-Si:H}$) silicon, which were developed in this
100 study. Combinations of a-Si:H and $\mu\text{c-Si:H}$ allow for a more precise adjustment of the PV
101 parameters and suffer less from stability issues under prolonged illumination (Staebler-
102 Wronski effect)²⁵ compared to their all-amorphous counterparts.²⁶ Former studies In fact, the
103 present study builds on a previous work,¹² in which the fundamental working principle of a
104 a-Si:H/a-Si:H tandem based PV-EC device has been demonstrated and validated by empirical
105 modeling. In the present work now, we developed a-Si:H/ $\mu\text{c-Si:H}$ / $\mu\text{c-Si:H}$ and a-Si:H/a-
106 Si:H/ $\mu\text{c-Si:H}$ triple and a-Si:H/a-Si:H/ $\mu\text{c-Si:H}$ / $\mu\text{c-Si:H}$ quadruple junction solar cells aiming
107 to provide higher STH efficiencies in PV-EC configuration and higher tunable excess
108 voltages to have a higher flexibility in choosing different catalyst materials with different
109 overpotential requirements. Extending beyond former studies on thin film silicon
110 multijunction photoelectrodes,^{10,15-17} the present work demonstrates the tunability of voltages
111 over a very wide range. Thereby, the variety of feasible applications in photoelectrochemical
112 systems is considerably extended. We used a-Si:H sub cells with different optical band gaps,
113 as well as $\mu\text{c-Si:H}$ absorber layers with improved stability against light-induced degradation
114 which leads to an improved solar cell performance. Particularly, the photocurrent density was
115 significantly improved (by 0.8 mA/cm²) by implementing microcrystalline silicon oxide ($\mu\text{c-SiOx:H}$)
116 as intermediate reflecting layers²⁷ and by carefully adapting the thicknesses of the
117 individual sub cells. The applicability of the developed solar cells as photocathodes in an
118 integrated PV-EC device is further demonstrated with thin Pt and Ni catalyst layers,
119 respectively on top of the solar cells for the HER and a RuO₂ counter electrode for the OER.
120 Additionally, the associated aspects of the PV-EC device performance were addressed. In
121 particular, the long-term durability as required for commercial applications has already been
122 emphasized previously.²⁸⁻³¹ Besides the electrochemical stability, the present study
123 furthermore investigates the aspects of catalysis and electrolyte dependence on the
124 performance of the developed multijunction Si photocathodes.

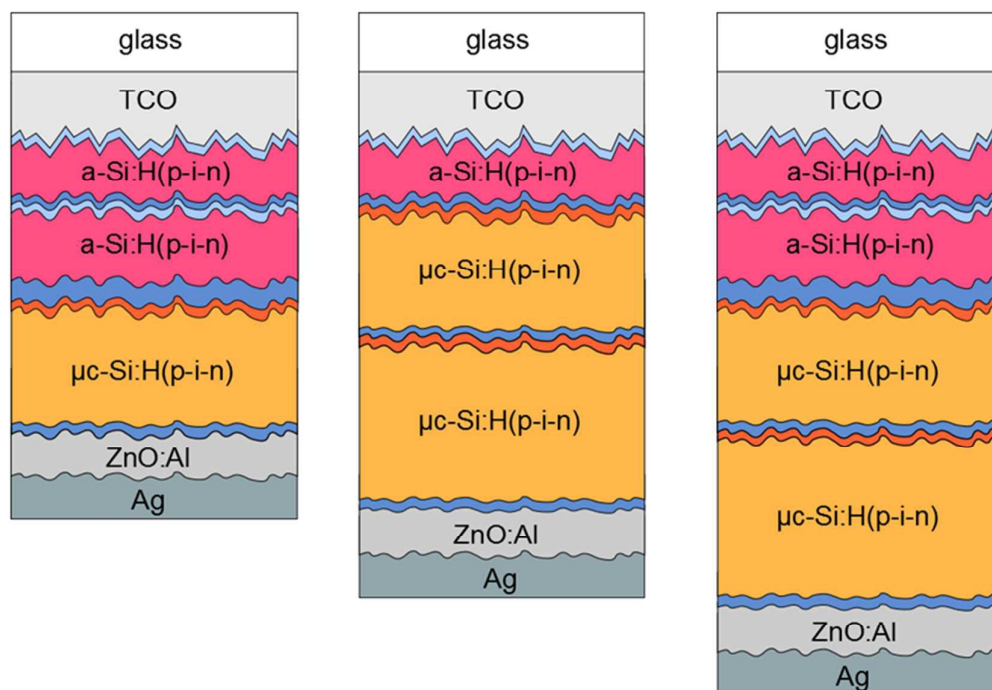
125 126 127 **II. Experimental Details**

128

129

A. Preparation of thin film silicon layers and solar cells

130 All thin film silicon layers were deposited by a plasma enhanced chemical vapor deposition
 131 technique in a multi chamber system. For the intrinsic absorber layers a mixture of silane
 132 (SiH_4) and hydrogen (H_2) gases was used. For the n- and p-type layers, trimethylborane
 133 (TMB), methane (CH_4), phosphine (PH_3), and carbon dioxide (CO_2) gases were added to the
 134 silane-hydrogen mixture. For $\mu\text{c-Si:H}$ intrinsic and p-type layer depositions an excitation
 135 frequency of 94.7 MHz was applied. For all a-Si:H layers an excitation frequency of 13.56
 136 MHz was applied. The triple and quadruple junction solar cells were made in stacked p-i-n
 137 superstrate configuration with a sputtered zinc oxide/silver (ZnO:Al/Ag) reflecting rear
 138 contact³² defining the area (1 cm^2) of the individual cells. For all intrinsic $\mu\text{c-Si:H}$ absorber
 139 layers a silane concentration (SC) of 5.0 %, defined as the ratio between the SiH_4 flow and the
 140 total gas flow, and a substrate deposition temperature (T_S) of $180 \text{ }^\circ\text{C}$ was chosen.²⁶ The
 141 intrinsic a-Si:H top and middle cell absorber layers were deposited at $130 \text{ }^\circ\text{C}$ with a SC of 4 %
 142 and at $180 \text{ }^\circ\text{C}$ with a SC of 10 %, respectively.⁹ The p- and n-type layers are the same for all
 143 fabricated solar cells and are deposited at a T_S of $180 \text{ }^\circ\text{C}$. The a-Si:H/a-Si:H/ $\mu\text{c-Si:H}$ triple
 144 cells were deposited on 100 cm^2 fluorine-doped tin dioxide ($\text{SnO}_2:\text{F}$) coated glass substrates
 145 (front contact) with a native texture (Asahi U). The a-Si:H/ $\mu\text{c-Si:H}$ / $\mu\text{c-Si:H}$ and quadruple
 146 cells were deposited on 100 cm^2 textured aluminum-doped ZnO coated glass substrates (front
 147 contact). Fig. 1 schematically shows the multijunction solar cell configurations investigated in
 148 this study.



149

150 Fig. 1. Schematic drawing of the a-Si:H/a-Si:H/ $\mu\text{c-Si:H}$ and a-Si:H/ $\mu\text{c-Si:H}$ / $\mu\text{c-Si:H}$ triple and
 151 a-Si:H/a-Si:H/ $\mu\text{c-Si:H}$ / $\mu\text{c-Si:H}$ quadruple junction solar cell structures in p-i-n configuration
 152 investigated in this study.

153

154

155

156 **Characterization of solar cells**

157 The solar cells were characterized by current–voltage (J – V) measurements at standard test
 158 conditions (100 mW/cm^2 , 25°C) using a double source (Class A) AM 1.5 sun simulator with
 159 an anti-reflection foil on top of the front glass.³³ Furthermore, spectral response measurements
 160 [quantum efficiency (QE)] of the multijunction solar cells were conducted using a
 161 monochromator in a wavelength range between 300 nm to 1100 nm. Individual sub cell QE s
 162 of the triple and quadruple cells were separately determined using LEDs and a spectrally
 163 filtered bias light from a tungsten lamp. Bias light intensities of approximately 1 mW/cm^2
 164 were used to saturate the respective sub cells, while the intensity of the probing light was
 165 around 1000 times lower. The corresponding wavelengths used for the saturation of the sub
 166 cells are presented in Table 1.

167 Table 1. Overview of the used light wavelengths for the saturation of the individual sub cells
 168 in triple and quadruple junction solar cells for the QE evaluation.

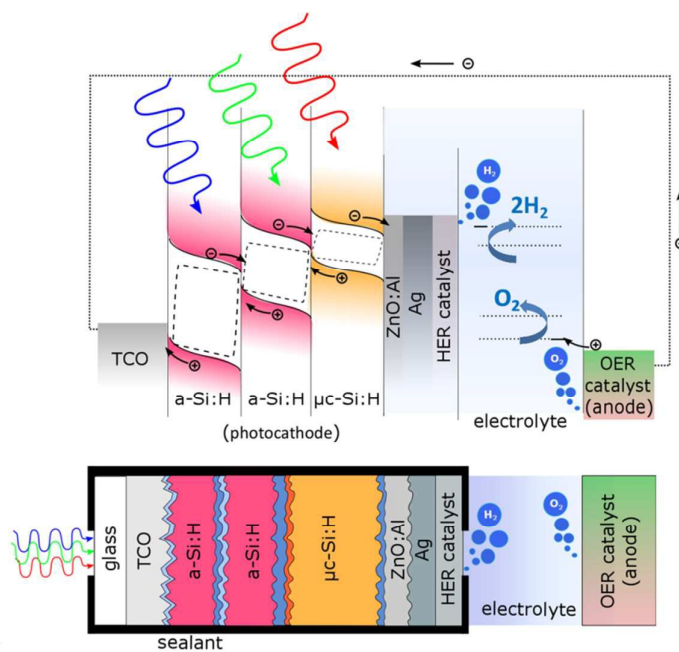
Cell type \ Measured sub cell	Top cell	Middle cell 1	Middle cell 2	Bottom cell
a-Si:H/ $\mu\text{c-Si:H}/\mu\text{c-Si:H}$	695 nm	765 nm and 470 nm	-	525 nm
a-Si:H/a-Si:H/ $\mu\text{c-Si:H}$	590 nm	780 nm and 400 nm	-	525 nm
a-Si:H/a-Si:H/ $\mu\text{c-Si:H}/\mu\text{c-Si:H}$	590 nm	780 nm and 400 nm	525 nm and 830 nm	625 nm

169 As an example, for the a-Si:H/ $\mu\text{c-Si:H}/\mu\text{c-Si:H}$ triple cell, light with 695 nm wavelength was
 170 used for the saturation of the middle and bottom cell assuring that the top cell, which
 171 photocurrent is intended to be measured, limits the current of the whole device. For the
 172 measurement of the bottom cell, light of 525 nm wavelength was used to saturate the top and
 173 the middle cell. In the case of the middle cell QE measurement, the top cell is saturated with a
 174 470 nm light and the bottom cell is saturated with 765 nm light.

175 **B. Photoelectrochemical measurements**

176 The integrated PV-EC device is schematically depicted as band diagram illustration in Fig. 2.
 177 It is composed of four main components: the multijunction solar cell (p-i-n type
 178 photocathode) to provide sufficient photovoltage and photocurrent for the water splitting
 179 reactions, a catalyst layer to enhance the HER, which is deposited on top of the solar cell at
 180 the photocathode/electrolyte interface, the electrolyte, which should provide high ionic
 181 conductivity, and an anode, coated with a catalyst to enhance the OER. The
 182 photoelectrochemical performance of the PV-EC devices was evaluated at room temperature
 183 in aqueous 0.1 M and 1 M KOH solutions using a two-electrode configuration.³⁴ The HER
 184 catalyst layer (Pt and Ni in this study) was deposited by electron beam evaporation with a
 185 thickness of around 150 nm on top of the Ag contact pads of the solar cell. In fact, the solar
 186 cell together with the attached HER catalyst compose the photocathode of the PV-EC device.

187 The photocathode-electrolyte contact area was defined by an O-ring sealing aperture and was
 188 0.5 cm^2 . For the OER catalyst, a RuO_2 coated titanium sheet was used as anode (15 g/m^2
 189 RuO_2 , 3 cm^2 active area, supplied by Metakem). Photocathode and anode were separated by a
 190 distance of 2 cm. White light photocurrent measurements were performed under simulated
 191 AM 1.5 solar illumination (100 mW/cm^2) using an Oriel LCS-100 solar simulator (model
 192 94011A) and an optical aperture of 0.5 cm^2 . Linear sweep voltammetry measurements were
 193 performed with a scan rate of 30 mV s^{-1} without stirring of the electrolyte. Electrical contact
 194 to the transparent conductive oxide (TCO) coated glass substrate, i.e. the front contact of the
 195 solar cell, was made by a silver paste. The PV-EC devices were illuminated through the glass
 196 substrate of the integrated solar cell (see Fig. 2), which offers the advantage that the light
 197 enters the photocathode through the TCO coated glass substrate without being attenuated by a
 198 surrounding medium (e.g. the electrolyte or gas bubbles). A major role in this configuration is
 199 governed by the metallic contact at the photocathode/electrolyte interface, which has to fulfill
 200 multiple requirements: (i) optical reflection of incident light back into the photocathode, (ii)
 201 protection of the photocathode from the electrolyte and undesired chemical reactions, and (iii)
 202 promotion of the catalytic reaction and a good electrical contact between the photocathode
 203 and the electrolyte. In this regard, a contact stack of ZnO:Al , Ag , and HER metal catalyst was
 204 used. The ZnO:Al/Ag double layer was used to ensure a good reflectivity of the incoming
 205 light, and thus allow for a high photocurrent. The thin metal layer deposited on top of the Ag
 206 layer was used as a catalyst for the HER.^{9,12,24}
 207 Nevertheless, for industrial applications a two-compartment set-up for the OER and HER,
 208 respectively separated through a membrane for quantitative gas amount evaluation is desirable
 209 and currently under construction. The configuration used in this study particularly aims to test
 210 prototype PV-EC devices based on our developed solar cells.



211

212 Fig. 2. Band diagram illustration of the PV-EC device configuration investigated in this study,
 213 with its components: the multijunction photocathode (as example a-Si:H/a-Si:H/μc-Si:H)
 214 under non-biased illumination condition, a HER catalyst layer at the photocathode/electrolyte

215 interface, the electrolyte, and the anode with the OER catalyst. The energy levels for the HER
 216 and OER and the respective reactions are indicated in the illustration. Hydrogen evolution
 217 occurs at the rear side of the photocathode and oxygen occurs at the anode side. $\Delta E = 1.23$ V is
 218 the thermodynamic potential required for water electrolysis at 25 °C. η_{HER} and η_{OER} indicate the
 219 overpotentials for the HER and OER, respectively.

220 III. Results and Discussion

221 A. Multijunction Solar Cells

222 The development of individual sub cells (a-Si:H and $\mu\text{c-Si:H}$ single junction solar cells) of a
 223 multijunction device has been addressed in detail elsewhere.^{9,24} The present study investigates
 224 the combination in triple and quadruple junction solar cells and exploits ways to improve the
 225 device efficiency in combination with high V_{OC} ranging from 2.0 V to 2.8 V. Due to
 226 requirements on the band gap sequence, the top and bottom cell absorber layers were made of
 227 a-Si:H (high band gap) and $\mu\text{c-Si:H}$, respectively, for all investigated multijunctions. For the
 228 middle cell absorber layers in triple junction solar cells either a-Si:H (lower band gap) or $\mu\text{c-Si:H}$
 229 Si:H were applied, which leads to different voltage and current matching conditions and
 230 represents the two development paths discussed below.

231 A1. a-Si:H/ $\mu\text{c-Si:H}$ / $\mu\text{c-Si:H}$ triple junction solar cells

232 A target for a-Si:H/ $\mu\text{c-Si:H}$ / $\mu\text{c-Si:H}$ triple junction solar cells was to achieve higher V_{OC}
 233 values than state-of-the-art a-Si:H/a-Si:H tandem junctions, i.e. above 1.9 V. Additional
 234 emphasis was put on photocurrent-matching of the individual sub cells and an increase in J_{SC}
 235 by integrating n-doped $\mu\text{c-SiO}_x\text{:H}$ layers.^{27,35,36} For the top cell absorber layer a high band gap
 236 a-Si:H material (1.95 eV \pm 25 meV) was chosen to increase the light incoupling and the V_{OC} .⁹
 237 Furthermore, the V_{OC} was increased by integrating nominally identical thin intrinsic a-Si:H
 238 buffer layers at the i-n interface of the $\mu\text{c-Si:H}$ sub cells. A similar approach were previously
 239 described for $\mu\text{c-Si:H}$ single junction solar cells.^{26,41} To evaluate the different routes, we
 240 investigated four different types of a-Si:H/ $\mu\text{c-Si:H}$ / $\mu\text{c-Si:H}$ cells (referred to as T1-T4):

- 241 • a reference solar cell fabricated without $\mu\text{c-SiO}_x\text{:H}$ layers and without n-i buffer layer
 242 (“T1”),
- 243 • a cell with $\mu\text{c-SiO}_x\text{:H}$ layers for middle (<n2>) and bottom cell (<n3>) without n-i
 244 buffer layer (“T2”),
- 245 • the same cell as T2, but with 30 nm n-i buffer layer for the bottom cell (“T3”),
- 246 • the same cell as T2 with a 30 nm buffer layers for the bottom and a 20 nm thin buffer
 247 layer for the middle cell (“T4”).

248 Table 2 summarizes the performance of these triple junction cells, including layer preparation
 249 and PV parameters of the solar cells.

250 Table 2. Overview of all relevant layer preparation and PV parameters (V_{OC} , J_{SC} , FF , and
 251 efficiency η) of a-Si:H/ $\mu\text{c-Si:H}$ / $\mu\text{c-Si:H}$ devices.

Cell no.	$\mu\text{c-SiO}_x\text{:H}$ <n2> and <n3>	n-i buffer layer	V_{OC} [mV]	J_{SC} [mA/cm ²]	FF [%]	V_{MPP} [mV]	J_{MPP} [mA/cm ²]	η [%]

	layers							
T1	w/o	w/o	1906	8.0	69.6	1598	6.6	10.6
T2	with	w/o	1895	8.3	70.8	1602	6.8	11.1
T3	with	bottom	1958	8.3	68.1	1596	6.9	11.1
T4	with	bottom and middle	1976	8.4	67.6	1590	7.1	11.2

252

253 The sub cells had a thickness of 160 nm for the top, 1200 nm for the middle, and 1600 nm for
 254 the bottom cell. As presented in Table 2, the integration of $\mu\text{c-SiO}_x\text{:H}$ as intermediate
 255 reflecting layers effectively increased the photocurrent density by 0.4 mA/cm^2 (T1 to T4).
 256 Through the integration of intrinsic a-Si:H buffer layers at the $\mu\text{c-Si:H}$ n-i interfaces the V_{OC}
 257 was increased by around 60 mV for one buffer layer (T3) and around 80 mV to 1976 mV for
 258 two buffer layers for middle and bottom cell (T4), along with a slight decrease in FF .
 259 Although the voltage at MPP was around 1.6 V for all cells, the current at MPP was increased
 260 by approx. 0.5 mA/cm^2 from cell T1 to T4. Overall this result exemplarily demonstrates that
 261 the V_{OC} can be tuned very systematically within a small voltage range, while the photocurrent
 262 at the MPP of the solar cell can be adjusted without impairing the device efficiency. This is
 263 relevant in particular for water splitting applications, as it allows to precisely adjust the PV
 264 parameters to the overpotential requirements of different catalyst materials.

265 Fig. 3 depicts the quantum efficiency measurement of the triple junction cell T4. The QE
 266 shows that all sub cells have very similar photocurrent densities of 8.0 mA/cm^2 , 8.2 mA/cm^2 ,
 267 and 8.3 mA/cm^2 as presented in Fig. 3.



268

269 Fig. 3. Quantum efficiency curves of a a-Si:H/ $\mu\text{c-Si:H}$ / $\mu\text{c-Si:H}$ triple junction device
 270 corresponding to cell T4 from Table 2. Sub cell current densities calculated from the QE -
 271 curves are placed near the related measurements and the total QE is displayed by the blue
 272 shaded area.

273 These values are slightly lower than the J_{SC} value quoted in Table 2, where an anti-reflection
 274 foil was additionally used during J - V measurements. From the total QE photocurrent (shaded

275 in blue) a slight dip between 500 nm and 650 nm is visible, which corresponds to reflection
276 losses at the intermediate reflecting/absorber layer interface.

277 A2. a-Si:H/a-Si:H/ $\mu\text{c-Si:H}$ triple junction solar cells

278 With the a-Si:H/a-Si:H/ $\mu\text{c-Si:H}$ triple junction cells the V_{OC} range was expanded to around
279 2.3 V. Furthermore, balanced and enhanced sub cell photocurrent densities were achieved by
280 introducing n-doped $\mu\text{c-SiO}_x\text{:H}$ layers for the top and bottom cells and a thicker n-doped $\mu\text{c-}$
281 $\text{SiO}_x\text{:H}$ intermediate reflecting (IR) layer after the a-Si:H middle cell.^{27,35,36} The latter ensures
282 that more short wavelength light is reflected back into the two (top and middle) a-Si:H sub
283 cells. Similar to the a-Si:H/ $\mu\text{c-Si:H}$ / $\mu\text{c-Si:H}$, this triple cell type used the same wide band gap
284 a-Si:H top cell absorber layer. For the middle cell an a-Si:H absorber layer with lower band
285 gap (1.91 eV \pm 25 meV) was applied. We compared three different a-Si:H/a-Si:H/ $\mu\text{c-Si:H}$
286 devices (referred to as T5-T7):

- 287 • a reference solar cell prepared without $\mu\text{c-SiO}_x\text{:H}$ n- and IR layers (“T5”),
- 288 • a cell with $\mu\text{c-SiO}_x\text{:H}$ n- and IR layers (“T6”), and
- 289 • the same cell as T6, but with adapted sub cell thicknesses such that a balanced
290 maximum current level is provided by each sub cells (“T7”).

291 The experimental data of the triple junction cells, in terms of QE measured photocurrent
292 densities of each individual sub cell, layer preparation (including layer thicknesses) and PV
293 parameters are presented in Table 3.

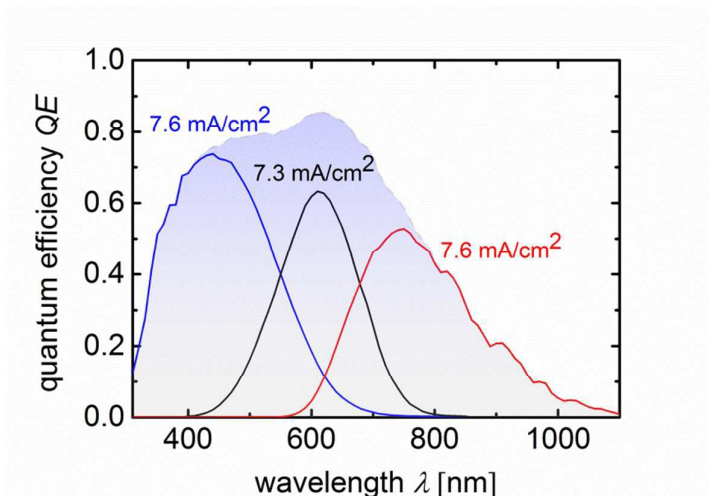
294 Table 3. Overview of all relevant photocurrent densities (for each individual sub cell), layer
295 preparation and PV parameters (V_{OC} , J_{SC} , FF , η) of a-Si:H/a-Si:H/ $\mu\text{c-Si:H}$ devices.

Cell no.	$\mu\text{c-SiO}_x\text{:H}$ <n1>, IR, and <n3>	$J_{\text{QE,top}}$ [mA/cm ²] (i-layer thickness) [nm]	$J_{\text{QE,mid}}$ [mA/cm ²] (i-layer thickness) [nm]	$J_{\text{QE,bot}}$ [mA/cm ²] (i-layer thickness) [nm]	V_{OC} [mV]	J_{SC} [mA/cm ²]	FF [%]	V_{MPP} [mV]	J_{MPP} [mA/cm ²]	η [%]
T5	w/o	7.3 (80)	6.8 (400)	7.4 (1200)	2269	7.8	72.3	1859	6.9	12.8
T6	with	7.4 (80)	7.1 (400)	7.4 (1200)	2272	8.3	71.2	1860	7.1	13.4
T7	with (matched)	7.6 (90)	7.3 (700)	7.6 (1800)	2279	8.6	69.2	1851	7.4	13.6

296

297 Again, the J_{SC} values are higher compared to the J_{QE} values measured from the QE
298 measurements because an anti-reflection foil was used for the J - V measurement. The
299 integration of $\mu\text{c-SiO}_x\text{:H}$ n-layers and IR layers significantly enhanced J_{SC} from 7.8 mA/cm²
300 (cell T5) to 8.3 mA/cm² (cell T6), mainly due to the increase of the middle cell photocurrent
301 density from 6.8 to 7.1 mA/cm². The current matched cell T7 provided the highest J_{SC} value
302 of 8.6 mA/cm² and a V_{OC} of 2279 mV. This shows that our approach results in an increase in
303 0.8 mA/cm² and 10 mV relative to cell T5. The good current-matching for cell T7 also results
304 in the slightly decreased fill factor. Overall an efficiency of 13.6 % was obtained along with a
305 V_{MPP} of 1851 mV with J_{MPP} of 7.1 mA/cm². Accordingly, in PV-EC device configuration,
306 overpotential losses up to 600 mV (1.85 V-1.23 V), which is in the range of state-of-the-art

307 precious metal catalyst materials for the HER and OER,^{39,40} are tolerable to operate the device
 308 near its maximum power point. The application of the multijunction solar cells in integrated
 309 water splitting device will be discussed in section 3.2. The quantum efficiency measurement
 310 of cell T7 is shown in Fig. 4.

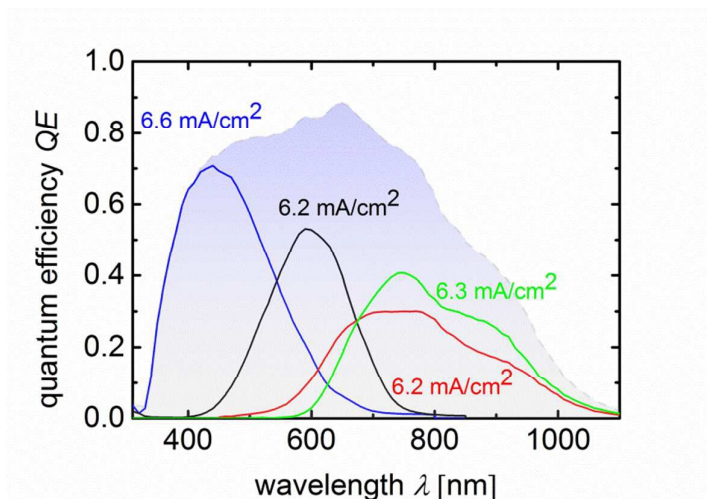


311

312 Fig. 4. Quantum efficiency curves of a a-Si:H/a-Si:H/μc-Si:H triple junction device
 313 corresponding to cell T7 from Table 3. Sub cell current densities calculated from the *QE*-
 314 curves are placed near the related measurements. The blue shaded area displays the total *QE*
 315 of the triple junction solar cell.

316 A3. a-Si:H/a-Si:H/μc-Si:H/μc-Si:H quadruple junction solar cells

317 To increase the flexibility in choosing catalyst materials for water splitting, e.g. catalytically
 318 less active non-precious metals, a large excess voltage (> 600 mV) is necessary. Open-circuit
 319 voltages of 2.8 V are feasible and were recently shown for quadruple cells.^{34,41,42} In contrast to
 320 intrinsic a-SiO_x:H used as top cell absorber layer⁴¹ or a-SiGe:H used as middle cell absorber
 321 material,³⁴ we applied the aforementioned wide band gap intrinsic a-Si:H material as top cell
 322 and the low band gap a-Si:H material as middle cell absorber layers. We used μc-SiO_x:H n-
 323 layers and integrated an IR layer between the middle a-Si:H and the first μc-Si:H sub cell. In
 324 order to match the sub cells in terms of the highest possible photocurrent, the thicknesses of
 325 each cell were systematically adjusted. The highest efficiency of 13.2 % ($V_{OC} = 2.802$ V, $J_{SC} =$
 326 6.8 mA/cm², and $FF = 69.5$ %) was obtained for the a-Si:H/a-Si:H/μc-Si:H/μc-Si:H quadruple
 327 cell with the respective intrinsic absorber layer thicknesses: a-Si:H top cell absorber: 80 nm,
 328 a-Si:H middle cell absorber: 400 nm, μc-Si:H middle cell absorber: 1500 nm, and μc-Si:H
 329 bottom cell absorber: 2500 nm. Fig. 5 displays the spectral response of the quadruple cell with
 330 the highest efficiency.



331

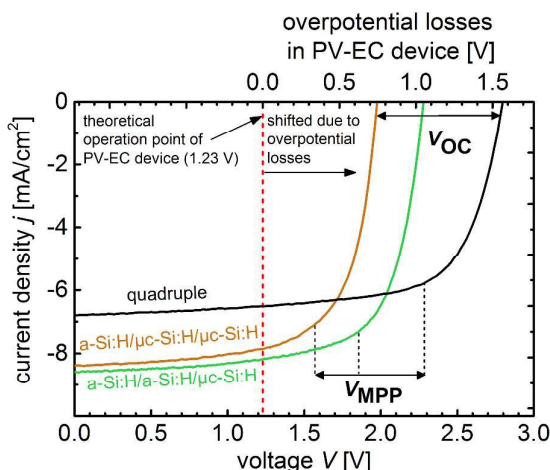
332 Fig. 5. Quantum efficiency curves of the a-Si:H/a-Si:H/μc-Si:H/μc-Si:H quadruple junction
 333 solar cell. Sub cell current densities calculated from the QE -curves are placed near the related
 334 measurements and the total QE is displayed by the blue shaded area.

335 In terms of water splitting, the high V_{MPP} of around 2278 mV ($J_{MPP} = 5.8 \text{ mA/cm}^2$) provides
 336 over 1 V of excess voltage and thus offers a lot of freedom in the choice of the catalyst
 337 material, which will be discussed in the following section.

338 Overall, the presented photovoltaic development deviates from prevalent routes, as we
 339 focused on high adjustable output voltages rather than on record electrical conversion
 340 efficiencies. Nevertheless, the conversion efficiencies of the triple and quadruple junction
 341 solar cells presented in this study are very close to the highest efficiencies reported for solar
 342 cells made of thin film silicon.⁴³ Fig. 6 summarizes the multijunction solar cell development
 343 and presents the J - V measurements of the best developed triple (cell T4 and T7 from Table 2
 344 and 3) and quadruple junction solar cells along with the V_{OC} (2.0 V to 2.8 V) and V_{MPP} (1.6 V
 345 to 2.3 V) range.

346 In real photoelectrochemical systems however, overpotential losses cause that the operation
 347 point (theoretically at 1.23 V, red vertical line in Fig. 6) is shifted towards more positive bias,
 348 as implied in Figure 6. Assuming that all PV parameters of the solar cells remain unchanged
 349 when they are integrated in a PV-EC device, Fig. 6 allows to illustratively predict the
 350 performance of PV-EC devices based on our developed solar cells. The operation
 351 photocurrent density of a PV-EC device can be read at the crossing point of the solar cell J - V
 352 with the operation point line at the respective overpotential from the upper x-axis. As can be
 353 deduced from Fig. 6, the a-Si:H/a-Si:H/μc-Si:H triple junction could provide a maximum
 354 operation photocurrent density of 8.2 mA/cm^2 when the PV-EC device would operate ideally,
 355 i.e. without any overpotential losses. When considering losses, the excess voltages become
 356 beneficial, as will be discussed in the following. Notwithstanding this, based on the presented
 357 photovoltaic results it is already possible to derive the practical performance limits of the
 358 state-of-the-art thin film silicon technology for water splitting applications.

359



360

361 Fig. 6. Current voltage curves of the developed triple, and quadruple junction solar cells based
 362 on a-Si:H and $\mu\text{c-Si:H}$. The achievable V_{OC} (2.0 V to 2.8 V) and V_{MPP} (1.6 V to 2.3 V) ranges
 363 are indicated, respectively. The J - V curves of the triple and quadruple junction solar cells are
 364 linked with the theoretical operation point of a PV-EC device at 1.23 V (red dashed vertical
 365 line, without overpotential losses). In real PV-EC devices this operation point is shifted due to
 366 overpotential losses, which are plotted on the upper x-axis.

367 B. Photovoltaic-biased Electrochemical Cells

368 B1. Calculation of solar-to-hydrogen efficiency

369 During operation the two electrodes (photocathode and anode) of the PV-EC device are
 370 shorted. The photocurrent density j_{op} at 0 V applied voltage can be used to estimate the STH
 371 efficiency of the PV-EC device using the following equation:⁴⁴

$$372 \eta_{\text{STH}} = \frac{\text{power out}}{\text{power in}} = \frac{\Delta E \times j_{\text{op}}}{\text{total integrated power input density}} \quad (1).$$

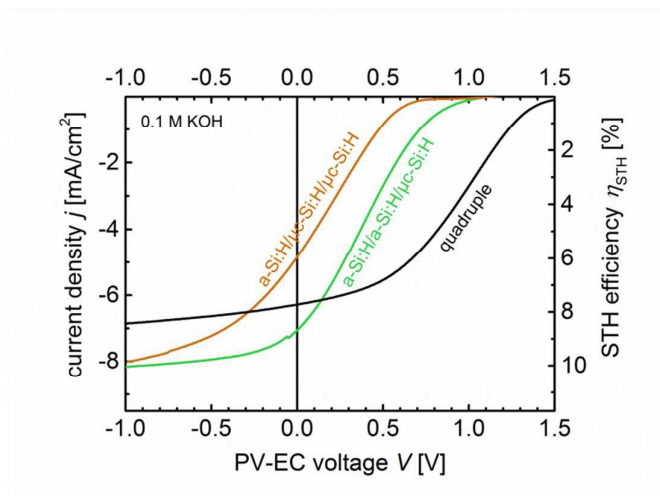
373 $\Delta E = 1.23$ V is the thermodynamic potential required for water electrolysis at 25 °C, j_{op} is the
 374 operating photocurrent density when no bias is applied, and the input power is the incident
 375 light intensity. Several different methodologies have been proposed in literature to evaluate
 376 the STH efficiencies of water splitting devices.⁴⁴⁻⁴⁷ One well-established method is described
 377 by Eq. (1).^{44, 45, 47} This calculation underlies the assumption that the measured photocurrent
 378 corresponds to the molecular hydrogen generation via proton reduction (100 % faradaic
 379 efficiency). The evaluation described above provides a consistent method for the comparison
 380 of the performance between various solar fuel production systems. The assumption of a
 381 faradic efficiency of 100% for the system under study was confirmed by a volumetric
 382 measurement of the evolved gases (see Fig. S1 and Fig. S2, in the ESI).

383 B2. Comparison of PV-EC devices based on triple and quadruple junction solar cells

384 Fig. 7 depicts the J - V measurements in 2-electrode configuration of the real PV-EC devices
 385 based on the multijunction solar cells developed in section A and measured in 0.1 M KOH.
 386 Apparently, the shape of the curves is different from the pure solar cell J - V presented in Fig.
 387 6. In particular the FF and V_{OC} are reduced, mainly because of the electrolyte resistance and

12

388 the overpotential losses at the electrode surfaces (Pt and RuO₂), respectively. The saturation
 389 photocurrent is slightly reduced compared with the pure J - V measurement on the solar cells,
 390 because for the PV-EC measurements no anti-reflection foil was used. However, light
 391 absorption and physics of the photogenerated charge carrier separation within the solar cell
 392 remain unaffected when used as photocathode in the PV-EC device.



393

394 Fig. 7. J - V measurements of PV-EC devices based on thin film silicon multijunction
 395 photocathodes with a 150 nm thick Pt layer as HER catalyst and a RuO₂ counter electrode for
 396 the OER reaction. The measurements are conducted in 0.1 M KOH at 50 mV/s.

397 Above all, the measurements show that the highest photocurrent at 0 V applied bias is
 398 provided by the a-Si:H/a-Si:H/ μ c-Si:H based PV-EC device. The device operates near its
 399 MPP at 7.1 mA/cm², which, according to Eq. (1), corresponds to a STH efficiency of 8.7 % in
 400 0.1 M KOH. For the a-Si:H/ μ c-Si:H/ μ c-Si:H based device further improvements in the fill
 401 factor of the solar cell (cell T4) have to be made in order to reach the MPP photocurrent in the
 402 short-circuit condition, and thus, achieve a higher STH efficiency. The operation point of the
 403 quadruple junction device lies at 6.2 mA/cm². Albeit the corresponding estimated 7.6 % STH
 404 efficiency is lower compared to the a-Si:H/a-Si:H/ μ c-Si:H device for the respective catalysts,
 405 the quadruple junction device operates in a relatively flat region of the J - V curve (current
 406 plateau region). Hence, this device provides a certain excess voltage, which offers a higher
 407 flexibility in choosing other non-precious catalyst materials, as will be discussed in the
 408 following section. The experimental data of the three PV-EC devices are summarized in Table
 409 4.

410 Table 4. Overview of the relevant parameters for the triple and quadruple based PV-EC
 411 devices using 0.1 M KOH as electrolyte, Pt as HER catalyst, and RuO₂ as OER catalyst. STH
 412 efficiencies are calculated based on the assumption of 100 % faradaic efficiency.

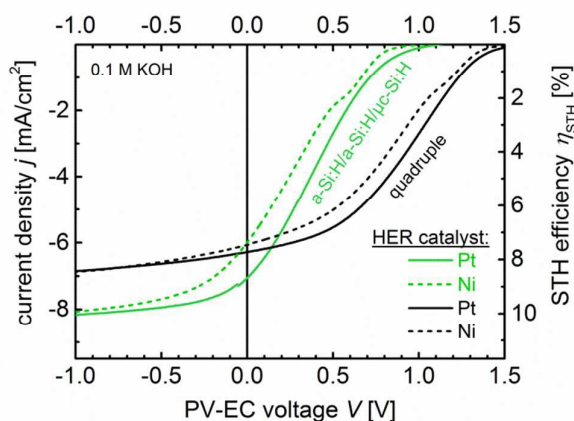
Photocathode	j_{op} [mA/cm ²]	η_{STH} [%]
a-Si:H/ μ c-Si:H/ μ c-Si:H	4.8	5.9
a-Si:H/a-Si:H/ μ c-Si:H	7.1	8.7
quadruple	6.2	7.6

413

414 B3. Pt and Ni as HER catalysts

415 From Fig. 7, it can be deduced that for an approx. 200 mV increase in overpotential losses the
 416 quadruple based device would exhibit a higher STH efficiency than its a-Si:H/a-Si:H/ $\mu\text{c-Si:H}$
 417 triple junction counterpart. To validate this result, we deposited Ni, instead of Pt on top of the
 418 quadruple and triple junction solar cell. Ni is catalytically less active than Pt, but as a non-
 419 precious and earth-abundant catalyst material it is alluring due to its cost-effectiveness.⁴⁸

420 In Fig. 8, the J - V measurements of the triple and quadruple junction based PV-EC devices
 421 with Pt and Ni layers as HER catalysts, respectively are compared.



422

423 Fig. 8. J - V measurements of PV-EC devices based on a-Si:H/a-Si:H/ $\mu\text{c-Si:H}$ triple and
 424 quadruple junction photocathodes with RuO_2 counter electrode for the OER reaction. For the
 425 HER reaction 150 nm of Ni (dotted curves) and Pt (solid curves) were deposited on top of the
 426 solar cells, respectively. The measurements were conducted in 0.1 M KOH at 50 mV/s.

427 As expected, the operation photocurrent density j_{op} for the Ni-coated triple and quadruple
 428 devices is lower compared to the platinized devices. But the a-Si:H/a-Si:H/ $\mu\text{c-Si:H}$ based
 429 device shows a significant decrease in j_{op} from 7.1 to 6.1 mA/cm^2 , while the quadruple based
 430 device only loses 0.1 mA/cm^2 by using a Ni catalyst layer instead of Pt and still operates in
 431 the current plateau region. Both Ni-coated devices exhibit nearly the same estimated STH
 432 efficiency of 7.5 % in 0.1 M KOH. However, the operation point of the triple junction based
 433 device lies in the steep slope of its J - V characteristics, where a slight deterioration of the
 434 device parameters, due to photocorrosion during long-term operation for instance, can
 435 significantly deteriorate the STH efficiency. The operation point of the quadruple based
 436 device on the other hand lies in the plateau of its J - V characteristics, and thus, is less sensitive
 437 to photovoltage or fill factor variations.

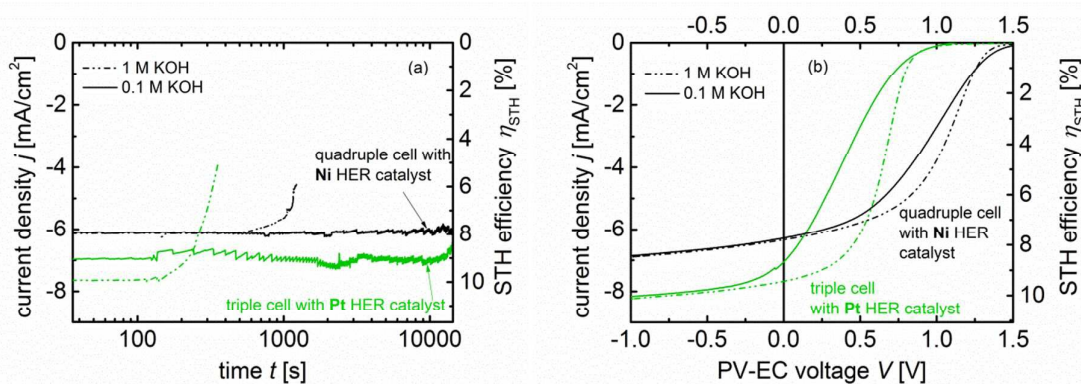
438

439 B4. Electrolyte concentration

440

441 The effect of the KOH electrolyte concentration on the stability and performance of the triple
 442 (a-Si:H/a-Si:H/ $\mu\text{c-Si:H}$) and quadruple junction based PV-EC devices are shown in Fig. 9 (a)

443 and (b), respectively. Fig. 9 (a) displays the photocurrent density at 0 V applied bias
 444 monitored over a prolonged period of time for the quadruple junction based device with a Ni
 445 HER catalyst and for the a-Si:H/a-Si:H/ μ c-Si:H based device with a Pt HER catalyst in 0.1 M
 446 and 1 M KOH, respectively.



447

448 Fig. 9. (a) Chronoamperometric stability measurement monitoring the long-term stability of
 449 the a-Si:H/a-Si:H/ μ c-Si:H and the quadruple junction based PV-EC devices with Pt and Ni
 450 catalyst layers, respectively, at 0 V applied bias on a logarithmic time scale. The
 451 measurements were conducted in 0.1 M (solid curves) and in 1 M KOH (dotted curves) under
 452 AM 1.5 illumination (100 mW/cm²). As a counter electrode for the OER reaction RuO₂ was
 453 used. (b) J - V measurements of the triple and quadruple junction based PV-EC devices in 0.1
 454 M (solid curves) and 1 M KOH (dotted curves). The measurements were conducted at a scan
 455 rate of 50 mV/s.

456 In 0.1 M KOH a stable photocurrent of approx. 6.1 mA/cm² and 7.0 mA/cm², respectively,
 457 was measured for both PV-EC devices over the course of 4 hours (approx. 15000 s). The
 458 periodical fluctuations in the photocurrent densities are caused by repetitive accumulation and
 459 detachment of H₂ bubbles at the photocathode surface. The measurements in 1 M KOH
 460 revealed that both devices did not operate longer than 1000 s. This result shows that a
 461 relatively small change in the pH value from approx. 13 to 14 has a significant effect on the
 462 stability of the PV-EC devices. In particular, pitting corrosion and delamination of the stacked
 463 metal layers at the solar cell-electrolyte interface prevented longer operation times. Here,
 464 adapted PV-EC device designs for robust water splitting operations need to be considered.³¹
 465

466 Notwithstanding this, in the case of the triple junction based device an increase of 0.7 mA/cm²
 467 in the operation photocurrent density j_{op} to 7.7 mA/cm² is observed when 1 M KOH is used as
 468 electrolyte solution instead of 0.1 M KOH. From Fig. 9 (b) it becomes apparent that this
 469 increase is caused by an improvement of the fill factor in the J - V curves of the triple junction
 470 based PV-EC devices. In fact, an increase in the electrolyte concentration reduces the series
 471 resistance of the complete PV-EC device, which leads to an improved fill factor. The effects
 472 of electrolyte resistance and other factors on the performance of PV-EC devices were
 473 investigated in more detail by modeling in a previous study.¹² According to Eq. (1) an
 474 impressive STH efficiency of 9.5 % can be estimated from the j_{op} of 7.7 mA/cm² for the triple
 475 based PV-EC device with Pt as HER and RuO₂ as OER catalyst. Please note that the solar-to-
 476 hydrogen efficiencies calculated via Eq. 1 represent an upper limit for the η_{STH} due to the
 477 assumption of unity faradaic efficiency.

478 Referring to a recently published overview of demonstrated STH conversion efficiencies,¹¹
479 this is the highest reported STH efficiency for an integrated monolithic thin film silicon based
480 photoelectrochemical device. STH efficiencies over 10 % would become feasible by using
481 anti-reflection foils to enhance the saturation photocurrents of the a-Si:H/a-Si:H/ μ c-Si:H solar
482 cell in the PV-EC device configuration by around 0.4 mA/cm² from 8.2 to 8.6 mA/cm² (see
483 Fig. 6). However, the issue of photocorrosion, particularly present for electrolyte
484 concentrations of or above 1 M, need to be solved at the same time. In this regard, the excess
485 voltage provided by the quadruple junction based device offers an additional advantage. As
486 apparent from Fig. 9 (a) and (b), the increase in electrolyte concentration does not affect the
487 operation photocurrent density of the device, which exhibits a j_{op} of 6.1 mA/cm² for the J - V
488 measurements conducted 0.1 M and 1 M KOH, respectively. This result can be understood,
489 because the device operates in the current plateau, where an improved fill factor does not
490 improve the current density (see Fig. 9 (b)). This overall shows that quadruple junction solar
491 cells not only promote the usage of cheaper catalyst materials, but also allow for the operation
492 in low-concentrated electrolytes without impairing the device efficiency, and thus, for an
493 increased long-term stability of the device and the catalysts.

494

495 In total, the presented PV-EC device concept in combination with the broad range of tunable
496 photovoltages offers an important toolbox for the investigation of related research challenges,
497 including catalyst development,⁴⁹ robust surface coating designs,³⁰ or integrated device
498 architectures.⁵⁰

499

500 IV. Summary

501 The present study outlined the important steps towards designing highly efficient
502 semiconductor structures and the presented results provide evidence that stable STH
503 efficiencies over 10 % are within the reach of thin film silicon based devices. We presented in
504 detail the development of triple and quadruple junction solar cells based on a-Si:H and μ c-
505 Si:H and demonstrated their applicability for efficient solar water splitting. The series-
506 connected multijunction cell configurations provided a wide range of achievable V_{OC} (2.0 V to
507 2.8 V) and V_{MPP} (1.6 V to 2.3 V) voltages. Additionally, we were able to systematically tune
508 the V_{OC} of the solar cells within a smaller voltage range (~50 mV) without impairing the
509 device efficiency, a feature which is highly important to compensate the losses occurring in
510 photoelectrochemical applications. Overall, by carefully adjusting the photocurrents of the
511 sub cells we achieved PV efficiencies of 13.6 % for triple and 13.2 % for quadruple junction
512 solar cells. The application in PV-EC devices showed that the a-Si:H/a-Si:H/ μ c-Si:H based
513 PV-EC device with Pt as hydrogen evolution catalyst and RuO₂ as oxygen evolution catalyst
514 exhibited 7.7 mA/cm² at 0 V applied bias, which corresponds to a solar-to-hydrogen
515 efficiency of 9.5 % (assuming a 100% Faradaic efficiency). The PV-EC device based on a
516 quadruple junction cell (a-Si:H/a-Si:H/ μ c-Si:H/ μ c-Si:H) exhibited enough excess voltage to
517 substitute Pt as precious metal catalyst by a more abundant material, such as Ni, and to work
518 in low-concentrated electrolyte solutions without impairing the solar-to-hydrogen efficiency.
519 With Ni as HER catalyst, this device provided 6.1 mA/cm² at 0 V applied bias over the course
520 of 4 hours.

521

522

523

524 **AUTHOR INFORMATION**525 **Corresponding Author**526 *E-mail: f.urbain@fz-juelich.de527 **Notes**

528 The authors declare no competing financial interests.

529 **ACKNOWLEDGMENT**

530 We thank U. Gerhards, L. Petter, W. Reetz, and H. Siekmann, for their contributions to this
531 work. The research is partly financially supported by the Deutsche Forschungsgemeinschaft
532 (DFG) Priority Programme 1613 (SPP 1613): Regeneratively produced fuels by light-driven
533 water splitting: Investigation of involved elementary processes and perspectives of
534 technologic implementation, and by the German Bundesministerium für Bildung und
535 Forschung (BMBF) in the network project: Sustainable Hydrogen (FKZ 03X3581A and FKZ
536 03X3581B). J. Ziegler, F. Yang, B. Kaiser, and W. Jaegermann acknowledge partial financial
537 support by the DFG Excellence Graduate School of Energy Science and Engineering (GSC
538 1070).

539

540

541

542

543

544

545

546

547

548

549 **REFERENCES**

550 [1] T. R. Cook, D. K. Dogutan, S. Y. Reece, Y. Surendranath, T. S. Teets and D. G. Nocera,
551 *Chem Rev.*, 2010, **110**, 6474-502.

552 [2] C. A. Grimes, O. K. Varghese and S. Ranjan, *Light, water, hydrogen: The solar generation*
553 *of hydrogen by water photoelectrolysis*, Springer, New York, 2008.

554 [3] A. J. Nozik and R. Memming, *J. Phys. Chem.*, 1996, **100**, 13061–13078.

555 [4] E. Miller, *White Papers on Materials for Photoelectrochemical Water Splitting*, DOE PEC
556 Working Group, 2013.

557

558 [5] Z. Li, W. Luo, M. Zhang, J. Feng and Z. Zou, *Energy Environ. Sci.*, 2013, **6**, 347–370.

559 [6] R. Memming, *Semiconductor Electrochemistry*, Wiley VCH, 2002.

560 [7] A. C. Nielander, M. R. Shaner, K. M. Papadantonakis, S. A. Francis and N. S. Lewis,
561 *Energy Environ. Sci.*, 2015, **8**, 16-25.

562 [8] B. Parkinson, *Acc. Chem. Res.*, 1984, **17**, 431–437.

563 [9] F. Urbain, K. Wilken, V. Smirnov, O. Astakhov, A. Lambertz, J.-P. Becker, U. Rau, J.
564 Ziegler, B. Kaiser, W. Jaegermann and F. Finger, *Int. J. Photoenergy*, 2014, **2014**, 249317.

565 [10] F. F. Abdi, L. Han, A. H. M. Smets, M. Zeman, B. Dam and R. van de Krol, *Nature*
566 *Communications*, 2013, **4**, 2195.

567 [11] J. W. Ager, M. R. Shaner, K. A. Walczak, I. D. Sharp and S. Ardo, *Energy Environ. Sci.*,
568 2015, accepted, DOI: 10.1039/C5EE00457H.

569 [12] F. Urbain, V. Smirnov, J.-P. Becker, U. Rau, J. Ziegler, B. Kaiser, W. Jaegermann and F.
570 Finger, *Sol. Energy Mat. Sol. Cells*, 2015, **140**, 275-280.

571

572 [13] T. J. Mills, F. Lin and S. W. Boettcher, *Physical Review Letters*, 2014, **112**, 148304.

573 [14] Z. Huang, J. R. McKone, C. Xiang, R. L. Grimm, E. L. Warren, J. M. Spurgeon, H.-J.
574 Lewerenz, B. S. Brunschwig and N. S. Lewis, *Int. J. Hydrogen Energy*, 2014, **39**, 16220-
575 16227.

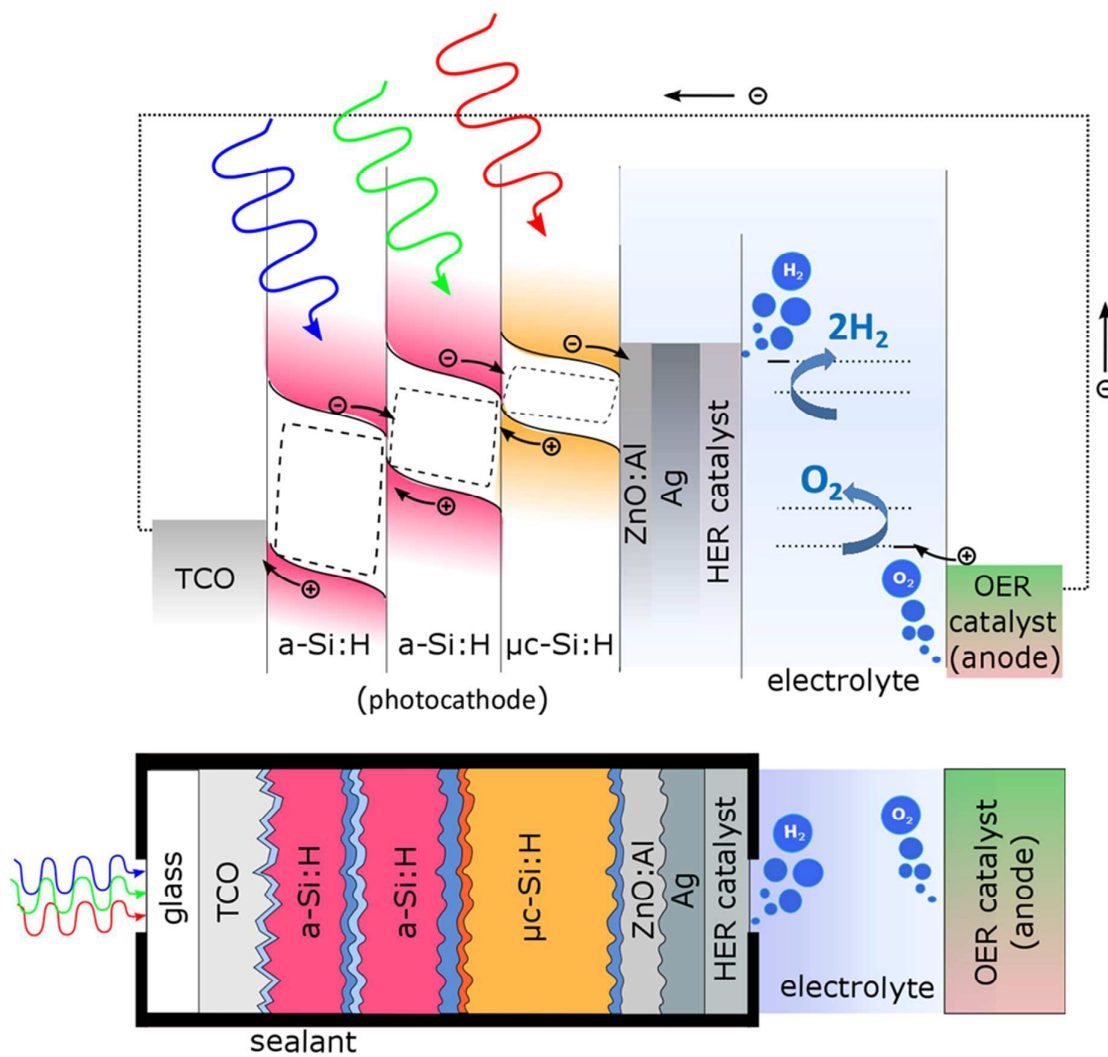
- 576 [15] A. E. Delahoy, S. C. Gau, O. J. Murphy, M. Kapur, J. O'M. Bockris, *Int. J. Hydrogen*
577 *Energy*, 1985, **10**, 113-116.
- 578 [16] S. Y. Reece, J. A. Hamel, K. Sung, T. D. Jarvi, A. J. Esswein, J. J. H. Pijpers and D. G.
579 Nocera, *Science*, 2003, **334**, 645-648.
- 580 [17] V. Cristino, S. Berardi, S. Caramori, R. Argazzi, S. Carli, L. Meda, A. Tacca and C. A.
581 Bignozzi, *Phys.Chem.Chem.Phys.*, 2013, **15**, 13083-13092.
- 582 [18] L. Han, I. A. Digdaya, T. W. F. Buijs, F. F. Abdi, Z. Huang, R. Lui, B. Dam, M. Zeman,
583 W. A. Smith and A. H. M. Smets, *J. Mater. Chem. A*, 2015, **3**, 4155-4162.
- 584 [19] R. E. Rocheleau, E. L. Miller and A. Misra, *Energy Fuels*, 1998, **12**, 3-10.
- 585 [20] O. Khaselev, A. Bansal and J. A. Turner, *Int. J. Hydrogen Energy*, 2001, **26**, 127-132.
- 586 [21] K. Fujii, S. Nakamura, M. Sugiyama, K. Watanabe, B. Bagheri and Y. Nakano, *Int. J.*
587 *Hydrogen Energy*, 2013, **38**, 14424-14432.
- 588 [22] T. J. Jacobsson, V. Fjällström, M. Sahlberg, M. Edoff and T. Edvinsson, *Energy Environ.*
589 *Sci.*, 2013, **6**, 3676-3683.
- 590 [23] C. R. Cox, J. Z. Lee, D. G. Nocera and T. Buonassisi, *PNAS*, 2014, **111**, 14057-14061.
- 591 [24] J. Luo, J.-H. Im, M. T. Mayer, M. Schreier, M. Khaja Nazeeruddin, N.-G. Park, S. D.
592 Tilley, H. Jin Fan and M. Grätzel, *Science*, 2014, **345**, 1593-1596.
- 593 [25] F. Finger, R. Carius, T. Dylla, S. Klein, S. Okur and M. Günes, *IEE Proc.-Circuits*
594 *Devices Syst.*, 2003, **150**, 300-308.
- 595 [26] F. Urbain, V. Smirnov, J.-P. Becker, U. Rau, J. Ziegler, B. Kaiser, W. Jaegermann and F.
596 Finger, *J. Mater. Res.*, 2014, **29**, 2605-2614.
- 597 [27] A. Lambertz, V. Smirnov, T. Merdzhanova, K. Ding, S. Haas, G. Jost, R. E. I. Schropp,
598 F. Finger and U. Rau, *Sol. Energy Mat. Sol. Cells*, 2013, **119**, 134-143.
599
- 600 [28] S. Hu, M. R. Shaner, J. A. Beardslee, M. Lichterman, B. S. Brunshwig and N. S. Lewis,
601 *Science*, 2014, **344**, 1005-1009.
602
- 603 [29] M. J. Kenney, M. Gong, Y. Li, J. Z. Wu, J. Feng, M. Lanza and H. Dai, *Science*, 2014,
604 **342**, 836-840.
605
- 606 [30] B. Mei, B. Seger, T. Pedersen, M. Malizia, O. Hansen, I. Chorkendorff and P. C. K.
607 Vesborg, *J. Phys. Chem. Lett.*, 2014, **5**, 1948-1952.
608
- 609 [31] N. A. Kelly, T. L. Gibson, *Int. J. Hydrogen Energy*, 2006, **31**, 1658-1673.
610

- 611 [32] W. Böttler, V. Smirnov, J. Hüpkens and F. Finger, *Phys. Status Solidi A*, 2012, **209**, 1144-
612 1149.
- 613 [33] C. Ulbrich, A. Gerber, K. Hermans, A. Lambert and U. Rau, *Prog. Photovolt: Res. Appl.*,
614 2013, **21**, 1672-1681.
- 615 [34] G. Hodes, *J. Phys. Chem. Lett.*, 2012, **3**, 1208–1213.
- 616 [35] V. Smirnov, A. Lambertz, S. Tillmanns and F. Finger, *Can. J. Phys.*, 2014, **92**, 932–935.
- 617 [36] S. Kirner, S. Calnan, O. Gabriel, S. Neubert, M. Zelt, B. Stannowski, B. Rech and R.
618 Schlatmann, *Phys. Status Solidi C*, 2012, **9**, 2145–2148.
- 619 [37] S. Hänni, M. Boccard, G. Bugnon, M. Despeisse, J.-W. Schüttauf, F.-J. Haug, F.
620 Meillaud and C. Ballif, *Phys. Status Solidi A*, 2015, **212**, 840–845.
621
- 622 [38] J.-W. Schüttauf, B. Niesen, L. Löfgren, M. Bonnet-Eymard, M. Stuckelberger, S. Hänni,
623 M. Boccard, G. Bugnon, M. Despeisse, F.-J. Haug, F. Meillaud and C. Ballif, *Sol. Energy*
624 *Mat. Sol. Cells*, 2015, **133**, 163–169.
- 625 [39] L. C. Seitz, Z. Chen, A. J. Forman, B. A. Pinaud, J. D. Benck and T. F. Jaramillo,
626 *ChemSusChem*, 2014, **7**, 1372–1385.
- 627 [40] C. C. L. McCrory, S. Jung, J. C. Peters and T. F. Jaramillo, *J. Am. Chem. Soc.*, 2013,
628 **135**, 16977-16987.
- 629 [41] F.T. Si, D. Yun Kim, R. Santbergen, H. Tan, R. A. C. M. M. van Swaaij, A. H. M.
630 Smets, O. Isabella and M. Zeman, *Appl. Phys. Lett.*, 2014, **105**, 063902.
631
- 632 [42] S. Kirner, S. Neubert, C. Schultz, O. Gabriel, B. Stannowski, B. Rech and R. Schlatmann,
633 *Jpn. J. Appl. Phys.*, 2015, **54**, 08KB03.
634
- 635 [43] M. Green, K. Emery, Y. Hishikawa, W. Warta and E. D. Dunlop, *Prog. Photovoltaics*,
636 2015, **23**, 1-9.
637
- 638 [44] Z. Chen, T. F. Jaramillo, T. G. Deutsch, A. Kleiman-Shwarsctein, A. J. Forman, N.
639 Gaillard, R. Garland, K. Takanabe, K. Heske, M. Sunkara, E. W. McFarland, K. Domen, E.
640 Miller, J. A. Turner and H. N. Dinh, *J. Mater. Res.*, 2010, **25**, 3-16.
- 641 [45] M. G. Walter, E. L. Warren, J. R. McKone, S. W. Boettcher, Q. Mi, E. A. Santori and N.
642 S. Lewis, *Chem. Rev.*, 2010, **110**, 6446-6473.
- 643 [46] Z. Chen, H. N. Dinh and E. Miller, *Photoelectrochemical Water Splitting*, Springer, New
644 York, 2013.

- 645 [47] R. H. Coridan, A. C. Nielander, S. A. Francis, M. T. McDowell, V. Dix, S. M. Chatman
646 and N. S. Lewis, *Energy Environ. Sci.*, 2014, accepted, DOI: 10.1039/C5EE00777A.
- 647 [48] J. R. McKone, E. L. Warren, M. J. Bierman, S. W. Boettcher, B. S. Brunschwig, N. S.
648 Lewis and H. B. Gray, *Energy Environ. Sci.*, 2011, **4**, 3573-3583.
- 649 [49] K. Maeda and K. Domen, *J. Phys. Chem. Lett.*, 2010, **1**, 2655-2661.
- 650 [50] B. Seger, I. E. Castelli, P. C. K. Vesborg, K. W. Jacobsen, O. Hansen and I.
651 Chorkendorff, *Energy Environ. Sci.*, 2014, **7**, 2397-2413.
- 652
- 653

Graphical Abstract

Bias-free solar water splitting is demonstrated using thin film silicon based triple and quadruple junction solar cells with solar-to-hydrogen efficiencies up to 9.5 %.



Broader context

Solar-driven water splitting, a process that mimics natural photosynthesis, provides a viable example of an ecofriendly energy concept as it converts solar energy into a storable and clean chemical fuel, namely hydrogen. To be competitive with fossil fuels or hydrogen production by other means, this process must however become highly efficient and low-cost. Integrated semiconductor based photoelectrochemical systems emerged as adequate candidates and have been attracting considerable interest among research groups worldwide. In the scientific literature, numerous studies have successfully demonstrated unbiased solar water splitting using Si based photovoltaic-electrochemical (PV-EC) devices. To maximize the solar-to-hydrogen efficiency, the photovoltaic cells, however, need to be specifically designed to match electrical parameters for water splitting. Therefore, the present study focuses on the tuning of both, the electrochemical and the photovoltaic parameters of integrated Si based PV-EC devices with respect to the water splitting requirements. We demonstrate the applicability of various types of multijunction photocathodes in PV-EC device configuration which provide a wide range of adjustable photovoltages from 2.0 to 2.8 V. Thereby, the variety of feasible applications and material combinations in photoelectrochemical systems is considerably extended, leading to a remarkable solar-to-hydrogen efficiency of 9.5 %.